Icarus 221 (2012) 481–494

Contents lists available at SciVerse ScienceDirect

Icarus

journal homepage: www.elsevier.com/locate/icarus

Magnetosphere–atmosphere coupling at Saturn: 1 – Response of thermosphere and ionosphere to steady state polar forcing

I.C.F. Müller-Wodarg [a,b,*], L. Moore [b], M. Galand [a,b], S. Miller [c], M. Mendillo [b]

[a] Space and Atmospheric Physics Group, Imperial College London, UK
[b] Center for Space Physics, Boston University, Boston, MA 02215, USA
[c] Atmospheric Physics Laboratory, University College London, UK

ARTICLE INFO

Article history:
Received 31 May 2012
Revised 12 August 2012
Accepted 28 August 2012
Available online 6 September 2012

Keywords:
Aeronomy
Saturn
Atmospheres, Dynamics
Ionospheres
Magnetospheres

ABSTRACT

We present comprehensive calculations of the steady state response of Saturn's coupled thermosphere–ionosphere to forcing by solar radiation, magnetospheric energetic electron precipitation and high latitude electric fields caused by sub-corotation of magnetospheric plasma. Significant additions to the physical processes calculated in our Saturn Thermosphere Ionosphere General Circulation Model (STIM–GCM) include the comprehensive and self-consistent treatment of neutral–ion dynamical coupling and the use of self-consistently calculated rates of plasma production from incident energetic electrons. Our simulations successfully reproduce the observed high latitude temperatures as well as the latitudinal variations of ionospheric peak electron densities that have been observed by the Cassini Radio Science Subsystem experiment (RSS). We find magnetospheric energy deposition to strongly control the flow of mass and energy in the high and mid-latitude thermosphere and thermospheric dynamics to play a crucial role in driving this flow, highlighting the importance of including dynamics in any high latitude energy balance studies on Saturn and other Gas Giants. By relating observed H_3^+ column emissions and temperatures to the same quantities inferred from simulated atmosphere profiles we identify a potential method of better constraining the still unknown abundance of vibrationally excited H_2 which strongly affects the H_3^+ densities. Our calculations also suggest that local time variability in H_3^+ column emission flux may be largely driven by local time changes of H_3^+ densities rather than temperatures. By exploring the parameter space of possible high latitude electric field strengths and incident energetic electron fluxes, we determine the response of thermospheric polar temperatures to a range of these magnetospheric forcing parameters, illustrating that 10 keV electron fluxes of 0.1–1.2 mW m^{-2} in combination with electric field strengths of 80–100 mV m^{-1} produce H_3^+ emissions consistent with observations. Our calculations highlight the importance of considering thermospheric temperatures as one of the constraints when examining the state of Saturn's magnetosphere and its coupling to the upper atmosphere.

1. Introduction

For the Gas Giants in our Solar System the coupling between magnetospheres and atmospheres is likely to play a key role for the energy and momentum balance of their thermospheres and ionospheres. While the same can be said to be the case at polar latitudes on Earth, its global energy balance due to closer proximity to the Sun is most of the time dominated by solar heating. Magnetospheric forcing on Earth is controlled by the interaction between the solar wind and magnetosphere via the Dungey cycle (Dungey, 1961), while on Jupiter the planet's rotation represents the primary generator of electric fields and driver of magnetospheric currents which ultimately lead to auroral emissions and enhanced ionospheric Pedersen and Hall currents (e.g., Clarke et al., 2004, Cowley et al., 2004, Bougher et al., 2005). On Saturn, evidence from auroral observations indicates that planetary rotation and solar wind both play a role, though their exact relative importance is still subject of debate (Clarke et al., 2009).

As first described by Hill (1979), corotation of magnetospheric plasma with a Gas Giant Planet such as Jupiter and Saturn is ultimately ensured by transfer of angular momentum from the upper atmosphere to the magnetosphere via a system of field-aligned Birkeland currents. In the magnetosphere the Birkeland current system is closed via radial currents in the equatorial plane which via $\mathbf{j} \times \mathbf{B}$ accelerations drive the plasma towards corotation. In the ionosphere the Birkeland currents close predominantly via field-perpendicular Pedersen currents which exert westward (against the sense of planetary rotation) acceleration on the

* Corresponding author at: Space and Atmospheric Physics Group, Imperial College London, UK.
E-mail address: i.mueller-wodarg@imperial.ac.uk (I.C.F. Müller-Wodarg).

0019-1035/$ - see front matter © 2012 Elsevier Inc. All rights reserved.
http://dx.doi.org/10.1016/j.icarus.2012.08.034

ionospheric plasma and, via ion–neutral collisions, onto thermospheric neutrals. The upper atmosphere at auroral latitudes where this coupling occurs will thus corotate to a lesser extent with the planet which, in the rotating frame of the planet, is manifested via westward wind velocities in the thermosphere. Furthermore, the Pedersen and Hall currents cause thermal heating, often referred to as Joule heating, due to the ionosphere's resistivity.

Using a radial profile of magnetospheric plasma velocities inferred from Voyager plasma observations and assuming fixed ionospheric conductances of 1 mho, Cowley et al. (2004) calculated the associated field aligned currents and resulting ionospheric Joule heating rates of around 2.5 TW per hemisphere, considerably larger than energy from the direct precipitation of electrons (globally $\leqslant$0.06 TW) and solar EUV heating (globally 0.15–0.27 TW) (Müller-Wodarg et al., 2006). Using simultaneous observations of fields and plasmas in Saturn's magnetosphere from Cassini and UV images from the Hubble Space Telescope (HST), Cowley et al. (2008) confirmed their earlier general results but revised the assumed conductances in the southern (summer-) hemisphere up from 1 to 4 mho.

Signatures of magnetosphere–atmosphere coupling are the auroral emissions that have been studied on Saturn in the EUV and FUV (emitted by H, H_2) and in the IR (emitted by H_3^+) (Kurth et al., 2009; Melin et al., 2011). The EUV/FUV emissions are associated primarily with energetic electron precipitation at energies ranging from 5 to 30 keV (Sandel et al., 1982; Gérard et al., 2004; Gustin et al., 2009; Lamy et al., 2010). Galand et al. (2011) studied the response of Saturn's ionosphere to precipitation of hard (10 keV) and soft (500 eV) electrons using their suprathermal electron transport code. They self-consistently calculated the ionisation rates and used these as input to the ionospheric model of Moore et al. (2010) to infer the resulting profiles of ion and electron densities. Galand et al. (2011) calculated Pedersen and Hall conductances as a function of precipitating particle energy and energy flux, deriving a square-root dependency of the conductances to energy flux for hard electrons. They also found the soft electrons to be important as a source of thermal electron heating but to have a minor influence upon the conductances.

The present study investigates magnetosphere–atmosphere coupling, specifically its effects on Saturn's polar thermosphere and ionosphere. Our goal is to present a comprehensive assessment of the effects of magnetospheric currents on temperatures, dynamics and composition. Using a global model of Saturn's coupled thermosphere and ionosphere (Moore et al., 2004, 2010; Müller-Wodarg et al., 2006; Galand et al., 2009, 2011), we self-consistently calculate for the first time the response of the coupled thermosphere–ionosphere system to a range of values for energetic particle precipitation flux and high latitude electric fields. Through comparisons of our calculations with observed thermospheric temperatures, we define the ranges of magnetospheric parameters that are consistent with atmospheric observations, thereby presenting a framework for using the atmosphere as an additional constraint in quantitatively describing Saturn's coupled magnetosphere/atmosphere system. Our study extends the work of Galand et al. (2011) in that it calculates the response of the neutral atmosphere to changing conductances, while their calculations had assumed a constant background neutral atmosphere. Our calculations show that thermospheric dynamics are crucial in determining the thermal structure in the polar atmosphere, highlighting the limitation of any 1-D thermal balance calculation which cannot include horizontal and resulting vertical dynamics.

In Section 2 we introduce the model and provide in Section 2.5 an overview of the simulation input parameters. Results for key physical quantities are presented in Section 3 alongside comparisons with observations. We provide a broader discussion of our findings including the limitations of our approach in Section 4.

2. The STIM model

The main tool in this study is the Saturn Thermosphere Ionosphere Model (STIM), a General Circulation Model (GCM) that treats the global response of Saturn's upper atmosphere to solar and magnetospheric forcing. Key physical quantities calculated by the code include global neutral temperatures, global densities of neutral and ion constituents, as well as neutral winds and ion drifts. In Sections 2.1, 2.2, 2.3, 2.4 we describe key components of STIM along with recent updates. We list the range of simulations presented in this study in Section 2.5.

2.1. Thermosphere–ionosphere GCM

Our simulations originate from two codes developed side-by-side but separately, namely, the Saturn Thermosphere GCM (Müller-Wodarg et al., 2006) and Saturn 1-D Ionosphere Model (Moore et al., 2004) which were subsequently fully coupled to form the Saturn Thermosphere Ionosphere Model (STIM). The thermosphere component globally solves the non-linear Navier–Stokes equations of momentum, continuity and energy on a spherical pressure level grid. The momentum equation includes terms such as pressure gradients, viscous drag, Coriolis acceleration, curvature accelerations and advection. The energy equation includes all processes of internal energy redistribution, such as advection, adiabatic heating and cooling as well as molecular and turbulent conduction. Solar EUV heating is calculated through explicit line-of-sight integration of solar irradiance attenuation (the Lambert–Beer Law), assuming solar spectra derived from the Thermosphere Ionosphere Mesosphere Energetics and Dynamics (TIMED)/Solar EUV Experiment (SEE) (Woods et al., 2005; Woods, 2008) and heating efficiencies of 50%, a value in agreement with estimates for Jupiter by Waite et al. (1983). While we include direct solar EUV heating in our calculations, it has a negligible influence on the energy balance of Saturn's thermosphere, as shown earlier by Müller-Wodarg et al. (2006). We show in Section 3 that the main importance of solar EUV radiation lies in its ionising role that leads to conductivities, Joule heating and ion drag which in turn affect the thermospheric energy budget and dynamics.

A new addition to the thermospheric energy equation is the inclusion of H_3^+ cooling, a process known to be important on Jupiter (Miller et al., 2006, 2010). At thermospheric temperatures typically found on Saturn (320–500 K, Nagy et al., 2009), we do not expect H_3^+ cooling to play an important role, but we included the process to be able to assess its importance for cases where polar magnetospheric heating raises temperatures above $\sim$500 K. We implemented globally the H_3^+ cooling rates of Miller et al. (2010) in the form of a parameterisation as a function of local thermospheric temperature and H_3^+ density.

The STIM GCM calculates the transport by winds and molecular and turbulent diffusion of key neutral species (H, H_2, He, CH_4, H_2O), following the procedures outlined by Müller-Wodarg et al. (2006). The global spherical grid has flexible resolution. For simulations in this study we assumed spacing in latitude and longitude of 2° and 10°, respectively, and a vertical resolution of 0.4 scale heights. Our time integration step was 5 s and we ran the code for 500 Saturn rotations to reach steady state.

Fully coupled chemically and dynamically to the thermosphere is a global ionosphere model based largely on the 1-D model of Moore et al. (2004). Neutral species undergo primary ionisation by solar EUV photons, assuming the solar spectra specified above. We include secondary ionisation by suprathermal photoelectrons using the parameterisation of Moore et al. (2009). The ions (H^+, H_2^+, H_3^+, He^+, CH_3^+, CH_4^+, CH_5^+, H_2O^+, H_3O^+) undergo reactions of charge exchange with neutral species and recombination with

electrons, following the chemical scheme of Moore et al. (2004), with additional reactions for hydrocarbon ions CH_3^+, CH_4^+ and CH_5^+, as given by Moses and Bass (2000). We assume $T_e = T_i = T_n$, a reasonable approximation as the relevant chemistry is not strongly influenced by T_e (Moore et al., 2008). We calculate ion velocities resulting from accelerations by magnetospheric electric fields, collisions with neutral gas particles and field-aligned diffusion (Moore et al., 2004).

The ion continuity equation is solved considering photo- and particle ionisation, chemical sources and sinks as well as transport by winds and diffusion. As shown by Moore et al. (2004), the ionosphere throughout the region studied here (near the main ionospheric peak) is largely in photochemical equilibrium, so dynamics have little influence on the ion distribution. This was predicted from comparison of transport and chemical lifetimes by Moore et al. (2004) and with the fully coupled model used here we confirm their finding. In particular, neutral winds are of little importance to the ion distribution. This is different from what is found in other atmospheres including those of Earth, Venus and Titan.

2.2. Water and vibrationally excited H_2

Two important components of the ionospheric photochemistry in STIM are the ion charge exchange reactions with ambient neutral water molecules and with vibrationally excited H_2. As shown by Moses and Bass (2000) and Moore et al. (2004), the dominant ion produced through solar ionisation in Saturn's ionosphere is H_2^+ which primarily results from solar radiation absorption by the dominant neutral species near the main ionospheric peak, H_2 (Galand et al., 2009). The H_2^+ produced is rapidly lost through charge exchange reactions with H_2, forming H_3^+, a shorter lived ion (relative to H^+) whose presence in the auroral regions of Saturn has been confirmed by ground-based observations (Stallard et al., 1999).

Another primary ion produced is H^+ which as an atomic ion recombines very slowly with free electrons, making it potentially longer-lived than H_3^+. As a result, H^+ becomes a key ion alongside H_3^+ despite the H^+ production rate near the ionospheric peak being lower by about an order of magnitude than that of H_2^+. In the absence of any further chemical sink, H^+ becomes the dominant ion on Saturn and due to its long lifetime barely varies with local time (Moore et al., 2004). A pattern of no appreciable diurnal behaviour is in contradiction to Saturn Electrostatic Discharge (SED) measurements (Kaiser et al., 1984; Fischer et al., 2011) and the dawn/dusk asymmetries observed by the Cassini Radio Science Subsystem (RSS) experiment (Nagy et al., 2006; Kliore, 2009). This dawn–dusk asymmetry suggests ionospheric recombination timescales of the dominant ion on Saturn's nightside to be of the order of a few hours, giving ions enough time to recombine on the nightside and their densities to be reduced in the dawn sector.

Two chemical processes have been investigated over the past decades which could effectively destroy H^+ ions, thereby reducing its (and the ionosphere's) chemical lifetime, generating local time variations in Saturn's ionosphere. These are the charge exchange reactions of H^+ with water,

$$H^+ + H_2O \rightarrow H_2O^+ + H \quad (1)$$

and with vibrationally excited H_2,

$$H^+ + H_2(v \geqslant 4) \rightarrow H_2^+ + H \quad (2)$$

The reaction rate of (1) assumed in STIM is given by $k_{H_2O} = 8.2 \times 10^{-9}\ cm^3\ s^{-1}$ (Anicich, 1993). Moore et al. (2006) presented a comparison of calculated ionospheric densities with low latitude Cassini RSS observations (Nagy et al., 2006) and concluded that the observed dawn–dusk asymmetry in the ionosphere at low latitudes was best reproduced by the model when imposing an external influx of neutral water molecules into the low- to mid-latitude upper atmosphere at a rate of $(0.5–1.0) \times 10^7\ cm^{-2}\ s^{-1}$. In their more extensive recent study, Moore et al. (2010) obtained a best fit between latitudinal profiles of Total Electron Content (TEC) in model and data when imposing the water flux as a Gaussian profile centered on the equator with a peak value of $0.5 \times 10^7\ cm^{-2}\ s^{-1}$ and full width half maximum (FWHM) of 23.5° latitude.

Fig. 1 shows the influx of water that we assume as upper boundary condition in the present study, as specified in Moore et al. (2010). Our model calculates the global transport of water molecules by diffusion and advection, and thereby their horizontal and vertical redistribution in the thermosphere. In imposing a peak water influx at equatorial latitudes, rather than a latitudinally more uniform distribution, we follow the notion that the bulk of gaseous water in the saturnian system would originate from the plumes of Enceladus and impact Saturn's upper atmosphere as a neutral constituent, thereby being unaffected by the magnetosphere and concentrated in the equatorial plane (Moore et al., 2006, 2010). Globally integrated, our assumed water influx amounts to $5 \times 10^{26}\ s^{-1}$. Assuming a water source rate from Enceladus of $1 \times 10^{28}\ s^{-1}$ (Jurac and Richardson, 2007; Cassidy and Johnson, 2010), this implies that we assume 5% of the produced water being lost to Saturn's atmosphere, slightly less than the values of 10% and 7% obtained by Jurac and Richardson (2007) and Cassidy and Johnson (2010), respectively.

For reaction (2) above, as discussed by Moore et al. (2010) and Galand et al. (2011), the basic reaction rate of H^+ with vibrationally excited H_2 has recently been updated to a value of $(0.6–1.3) \times 10^{-9}\ cm^3\ s^{-1}$ (Huestis, 2008). However, a large uncertainty remains in the fractional abundance of $H_2(v \geqslant 4)$ required for the reaction to proceed. Moore et al. (2010) defined an "effective" reaction rate (k_1^*), the product of the rate k_1 for reaction (2) and the volume mixing ratio, χ, of $H_2(v \geqslant 4)$ relative to H_2 : $k_1^* = k_1 \cdot \chi(H_2(v \geqslant 4))$ [$cm^3\ s^{-1}$]. Thus the uncertainty in the population of vibrationally excited H_2 manifests itself in the reaction rate k_1^* of reaction (2).

Moore et al. (2010), in the light of additional Cassini RSS observations, revisited their k_1^* rate and concluded that the best fit between model and observations was obtained when multiplying the original reaction rate of Moses and Bass (2000) by a factor of 0.125 which, with a revised average base reaction rate (from $k_1 = 2 \times 10^{-9}$ to $k_1 = 1 \times 10^{-9}\ cm^3\ s^{-1}$) (Huestis, 2008), corresponds effectively to a reduction of the assumed volume

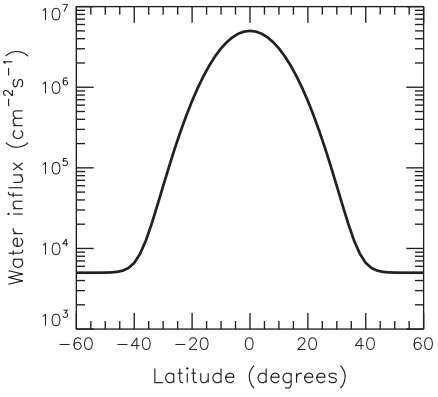

Fig. 1. Water influx imposed at the upper boundary of the vertical grid of STIM in all simulations presented in this study. For numerical stability a minimum base level influx is assumed poleward of ~40° in both hemispheres, but ignored in the ionospheric photochemistry calculations at those latitudes.

mixing ratio of $H_2(v \geqslant 4)$ by a factor of 4 with respect to that assumed by Moses and Bass (2000). For a more detailed discussion see Moore et al. (2010) and Galand et al. (2011).

The auroral region, which is the focus of the present study, is subject to energetic electron precipitation from Saturn's magnetosphere. We expect such precipitation to enhance the population of vibrationally excited H_2. As a result, we have assumed a $H_2(v \geqslant 4)$ abundance of twice the value assumed by Moses and Bass (2000). This approach was also followed by Galand et al. (2011). We have adopted this value globally, even though $H_2(v \geqslant 4)$ abundances are expected to be lower at non-auroral latitudes. Tests with STIM that we carried out for this study have revealed that such variations of $H_2(v \geqslant 4)$ at low and mid latitudes have little influence on the overall response of the thermosphere–ionosphere system to auroral forcing.

2.3. Ion drag and Joule heating

Key new additions to the thermospheric component of STIM with respect to that of Müller-Wodarg et al. (2006) are the inclusion of dynamical (momentum) coupling between the thermospheric neutrals and ionospheric ions and self-consistent calculations of Joule heating. In the absence of an external electric field, ions are constrained in their motion by the magnetic field. The neutral gases have collisional interactions with ions leading to a viscous-type force damping the motion of the neutral gases relative to that of the ions. When an external electric field is present, the ions are accelerated and the same collisional interaction leads to an acceleration of the neutral gases in the direction of ion motion. This latter interaction becomes important at auroral latitudes where an electric field is present. The ion drag term can, in general, be expressed as

$$\mathbf{a}_{ni} = -\nu_{ni}(\mathbf{u} - \mathbf{v}) \tag{3}$$

where $\mathbf{a}_{ni}$ denotes the acceleration due to neutral–ion collisions in the atmosphere, ν_{ni} is the neutral–ion collision frequency and $\mathbf{u}$, $\mathbf{v}$ are the neutral and ion velocities, respectively. In our model we implement the ion drag term in a different form, following the procedure used by Fuller-Rowell and Rees (1981), whereby the ion drag term is instead expressed as a function of the current density $\mathbf{J}$ in the ionosphere:

$$\mathbf{a}_{ni} = -\nu_{ni}(\mathbf{u} - \mathbf{v}) = \frac{1}{\rho}\mathbf{J} \times \mathbf{B} \tag{4}$$

where $\mathbf{B}$ denotes the ambient magnetic field in Saturn's ionosphere (Davis and Smith, 1990), and ρ is the atmospheric neutral mass density. In the simulations presented here, we enforced hemispheric symmetry in the magnetic field.

We calculate the current density $\mathbf{J}$ by using a generalisation of Ohm's law

$$\mathbf{J} = \underline{\sigma} \cdot (\mathbf{E} + \mathbf{u} \times \mathbf{B}) \tag{5}$$

where $\underline{\sigma}$ denotes the 3×3 conductivity tensor, $\mathbf{E}$ is an externally applied electric field (or internal polarisation field) and $\mathbf{u} \times \mathbf{B}$ represents the dynamo field. Thus, $(\mathbf{E} + \mathbf{u} \times \mathbf{B})$ is the electric field in the neutral rest frame. Following Rishbeth and Garriott (1969), we assume the concept of layer conductivities, whereby the conducting layer is assumed to have a limited vertical extent and may thus instead be expressed as a 2×2 tensor in the horizontal (latitudinal, zonal), given by

$$\underline{\sigma} = \begin{bmatrix} \sigma_P / \sin^2(I) & \sigma_H / \sin(I) \\ -\sigma_H / \sin(I) & \sigma_P \end{bmatrix} \tag{6}$$

Here, σ_P and σ_H denote the Pedersen and Hall conductivities, respectively, and I is the dip angle of the magnetic field $\mathbf{B}$. We calculate σ_P and σ_H self-consistently in the model at every grid point. Combining the 2-D version of (5) with (6) yields expressions for the latitudinal (j_θ) and longitudinal (j_ϕ) components of the current density as

$$j_\theta = \frac{\sigma_P}{\sin^2(I)}(E_\theta + u_\phi B_r) - \frac{\sigma_H}{\sin(I)}(-E_\phi + u_\theta B_r) \tag{7}$$

and

$$j_\phi = \sigma_P(E_\phi - u_\theta B_r) - \frac{\sigma_H}{\sin(I)}(E_\theta + u_\phi B_r) \tag{8}$$

where E_θ and E_ϕ denote meridional and zonal components of the electric convection or polarisation field, u_θ and u_ϕ are the meridional and zonal neutral wind components and B_r is the radial magnetic field. With Eq. (4) we obtain for the meridional and zonal ion drag acceleration terms the expressions

$$a_{ni,\theta} = \frac{1}{\rho} j_\phi \cdot B_r \tag{9}$$

and

$$a_{ni,\phi} = -\frac{1}{\rho} j_\theta \cdot B_r \tag{10}$$

which are added to the neutral wind momentum equation of Müller-Wodarg et al. (2006). The above implementation is consistent with that commonly used by General Circulation Models for Earth, such as the Coupled Thermosphere Ionosphere Model (CTIM) by Fuller-Rowell et al. (1996). While the above treatment assumes the layer conductivity concept, which neglects vertical currents, we have in a test version of STIM also implemented the ion drag term in its more generalised form using the full 3×3 conductivity tensor and found almost identical results. In the interest of simplicity and computing speed we have thus retained the 2×2 treatment in our model.

When currents flow in the ionosphere, an environment which is not perfectly conducting, resistive heating occurs, a process often referred to as Joule heating. Following the treatment of Fuller-Rowell and Rees (1981), we express the rate of Joule heating per unit mass using the relation

$$q_{Joule} = \frac{1}{\rho}(\mathbf{J} \cdot \mathbf{E}) = \frac{1}{\rho}(j_\theta E_\theta + j_\phi E_\phi) \tag{11}$$

Note that the electrical current $\mathbf{J}$ in the Joule heating term (Eq. (5)) includes the effect of neutral winds. Physically this means that the above expression for Joule heating consists of two components, the thermal heating of the atmosphere by electrical currents and the change of kinetic energy of the atmospheric gases which results from the momentum change due to ion drag (Eqs. (9) and (10)). Sometimes this latter component of heating is referred to as "ion drag heating". While the thermal heating by currents, q^*_{Joule}, can only be a positive quantity, the ion drag heating, q_{Joule}, can also attain negative values, implying loss of kinetic energy of the neutral atmosphere (Vasyliũnas and Song, 2005).

The Joule heating expression (Eq. (11)) is added to the neutral gas energy equation of Müller-Wodarg et al. (2006). The ion drag and Joule heating terms are thus calculated self-consistently in STIM, assuming a given external electric field $\mathbf{E}$ and auroral electron precipitation. This electric field originates from the departure of regions in Saturn's magnetosphere from corotation due to plasma production from internal sources. Thus $\mathbf{E}$ represents in our calculations a key parameter determining the coupling between magnetosphere and ionosphere. In a fully two-way coupled ionosphere–magnetosphere model, the value of $\mathbf{E}$ would change in response to atmospheric conditions, but we currently do not include this feedback in our model and define a fixed value of $\mathbf{E}$ based on calculations of Cowley et al. (2004).

2.4. Auroral electron precipitation

At polar latitudes, Saturn is known to possess auroral ovals which have been observed in the UV (Judge et al., 1980; Clarke et al., 1981; Gustin et al., 2009; Lamy et al., 2009), IR (Geballe et al., 1993; Stallard et al., 1999) and at visible wavelengths, as reviewed by Kurth et al. (2009). They are signatures of magnetosphere–ionosphere–thermosphere coupling processes, such as precipitation of energetic electrons and ions into the upper atmosphere, yielding ionisation, excitation, dissociation and heating. Particle ionisation processes exceed solar primary and secondary ionisation in the auroral regions. Ionisation at auroral latitudes due to precipitating suprathermal electrons thus plays a key role not only locally, but more globally due to the currents that can then flow, which in turn substantially affect the global energy balance.

To account for auroral particle ionisation processes, we calculate ionisation rates from suprathermal magnetospheric electrons using the electron transport model of Galand et al. (2011). Populations with a mean energy of 10 keV have been identified at Saturn in Voyager Ultraviolet Spectrometer (UVS), Hubble Space Telescope (HST), Cassini Plasma Spectrometer (CAPS) and Cassini Ultraviolet Imaging Spectrograph (UVIS) observations (Sandel et al., 1982; Gérard et al., 2004; Grodent et al., 2010). While we have the option of specifying any electron population in our model, we have chosen for this study to focus on 10 keV electrons. Additionally, we can independently specify the latitudinal distribution as well as any local time variations of the energy flux. The production rate resulting from the incident electron population is proportional to the assumed energy flux.

2.5. Simulation settings

In simulating the response of Saturn's coupled thermosphere–ionosphere system to magnetospheric forcing, we varied two key parameters in the model, namely, the energy flux of precipitating auroral 10 keV electrons and the auroral electric field strength.

Table 1
Summary of STIM GCM simulations discussed in this study. The auroral electron energy flux is for 10 keV electrons incident at 78° latitude. While all simulations assume this flux to vary with local time, as shown in Fig. 3 (black line), the table gives diurnally-averaged values. Peak electron fluxes near 08:00 local time are roughly a factor of 2 times the values given above. The listed electric field strengths are peak field strengths, attained near 78° latitude (see Fig. 2). Simulation R19 is the same as R15 in terms of auroral forcing, but assumes southern hemisphere summer solstice conditions. All simulations were run to steady state for 500 Saturn rotations.

Run code	Peak electric field strength (mV m^{-1})	Incident electron energy flux (local time averaged) (mW m^{-2})	Season
R1	95	0.07	Equinox
R2	85	0.07	Equinox
R3	76	0.07	Equinox
R4	95	0.12	Equinox
R5	85	0.12	Equinox
R6	76	0.12	Equinox
R7	95	0.17	Equinox
R8	85	0.17	Equinox
R9	76	0.17	Equinox
R10	95	0.22	Equinox
R11	85	0.22	Equinox
R12	76	0.22	Equinox
R13	95	0.62	Equinox
R14	85	0.62	Equinox
R15	76	0.62	Equinox
R16	95	1.24	Equinox
R17	85	1.24	Equinox
R18	76	1.24	Equinox
R19	76	0.62	Solstice

Table 1 provides a summary of all simulations, which will hereafter be referred to by their run codes (R1–R19).

We have run all simulations for solar minimum conditions (May 15, 2008), identical to the fluxes used by Galand et al. (2009, 2011). Simulations R1–R18 assume equinox conditions, while R19 is identical to R15 but for southern hemisphere summer conditions. We find however the overall seasonal variations in Saturn's upper atmosphere outside of the auroral regions to be of secondary importance only. All simulations were run to steady state for 500 Saturn rotations. While the ionosphere reaches steady state conditions considerably earlier, the thermosphere is characterised by long thermal time scales, thus requiring long run times before a steady state is reached. Even so, we note that no evidence is available to determine whether or not Saturn's upper atmosphere is in thermal equilibrium.

Fig. 2 shows the azimuthal (equatorward) electric field strength that we applied in all simulations. The (co-)latitude variations are consistent with calculations by Cowley et al. (2004) but we chose to vary the peak electric field strength from a maximum value equal to that of Cowley et al. (2004) ($E \leqslant 95$ mV m^{-1}, solid line) to scalings of 0.9 and 0.8 times their value ($E \leqslant 85$ mV m^{-1} (dotted) and $E \leqslant 76$ mV m^{-1} (dashed), respectively). In applying these scalings we explore the sensitivity of the atmosphere to uncertainties and any variation in the electric field strength. The field is applied symmetrically in both hemispheres (pointing southward in the northern hemisphere and northward in the southern hemisphere) and assumed independent of local time and longitude. The black box in Fig. 2 indicates the location of maximum precipitating energetic electron flux assumed in this study. It coincides with the location of sudden change in the degree of corotation. This shear may contribute towards the acceleration of the particles into the atmosphere (Cowley et al., 2004). The electric field strength mapped into the polar upper atmosphere is effectively a measure of the degree of corotation of plasma in Saturn's magnetosphere. A lower electric field strength implies a higher degree of corotation for any given value of conductance. While not a free parameter *per se*, enough uncertainties in the observed degree of plasma corotation in Saturn's magnetosphere (Stallard et al., 2004) and in the modelling of associated electric fields justify investigating the atmosphere response to variations of **E** within ≈ 20%. In reality

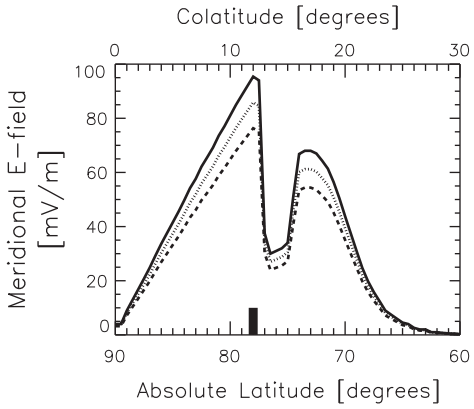

Fig. 2. Azimuthal (equatorward) electric field strength applied in simulations of this study. The solid line represents the field strength of Cowley et al. (2004), the dotted and dashed lines represent cases where the field strength of Cowley et al. (2004) was multiplied by 0.9 and 0.8, respectively. The field is applied symmetrically in both hemispheres (pointing southward in the northern hemisphere and northward in the southern hemisphere) and assumed independent of local time and longitude. The black box indicates the location of maximum precipitating energetic electron flux assumed in this study. It coincides with the location of sudden change in the degree of corotation. This shear is may contribute towards the acceleration of the particles into the atmosphere (Cowley et al., 2004).

the electric field will be more complex, including a zonal field component as well as longitude, latitude and temporal variations, but this is a reasonable first attempt.

The ionospheric plasma densities, and thereby Pedersen and Hall conductivities in the auroral region, are primarily controlled by the second parameter we vary, the incident electron energy flux. We assume a single population of electrons (10 keV), though in reality other energies are also present. We assume five different levels of electron energy flux which we allow to vary with local time. Local time-averages of the fluxes we assumed are listed in Table 1 as 0.07, 0.12, 0.17, 0.22, 0.62 and 1.24 mW m^{-2}.

The black line in Fig. 3 shows the local time variation of incident electron energy flux that we assume for the representative case of simulation R15 (see Table 1) at the latitude of maximum incident flux (78° in both hemispheres, see also black marker in Fig. 2). Fluxes in Fig. 3 vary from 0.03 mW m^{-2} at midnight to 1.3 mW m^{-2} at 08:00 h Solar Local Time (SLT). These local time variations are consistent with those inferred from Hubble Space Telescope (HST) auroral observations in the UV analysed by Lamy et al. (2009), scaled to our assumed average incident flux of 0.62 mW m^{-2} in R15 and to different averages for other simulations, as listed in Table 1. The local time dependence of the incident electron flux is combined in the model with a latitudinal Gaussian weighting function centered around 78° latitude, assuming a FWHM of 1.4°.

In response to particle precipitation and associated ion production rates, the self-consistently calculated ionospheric plasma densities are locally enhanced, generating an increase in Pedersen and Hall conductances as well as thermal Joule heating. The red curve of Fig. 3 shows the resulting Pedersen conductances which range from 5 mho at 00:40 h SLT to 16.7 mho at 08:40 h SLT, with an average of 11.5 mho. Conductances at Saturn are considerably larger than those at Jupiter due to the weaker magnetic field at Saturn. Note the 40 min SLT (corresponding to ~17 min real time) delay in local time between the maximum in precipitation and that in conductances. This delay, identified also by Galand et al. (2011) at similar magnitude, is associated with photochemical lifetimes in the ionosphere.

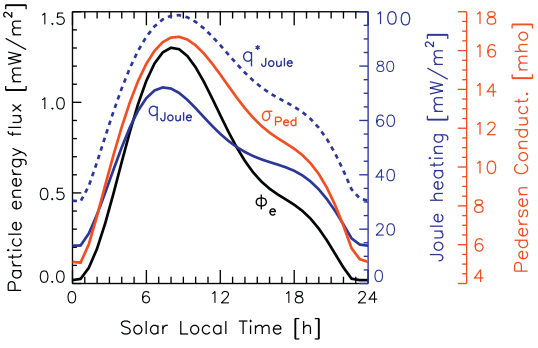

Fig. 3. Key auroral parameters in simulation R15 (see Table 1). The black line denotes energy flux, Φ_e, of incident 10 keV electrons at 78° latitude, with a local time-averaged value of 0.62 mW m^{-2}. The assumed local time variations are consistent with those inferred from auroral observations by Lamy et al. (2009). The incident electrons ionise Saturn's thermosphere at the rates calculated by Galand et al. (2011), leading to Pedersen conductances, σ_{Ped}, shown here as the red line which range from 5 to 17 mho, with a local time-average of 11.5 mho. Applying an external equatorward electric field with a peak strength of 76 mV m^{-1} (dashed line in Fig. 2) leads to the height-integrated Joule heating rates shown as blue lines. The dashed blue line represents the thermal Joule heating, while the solid blue line represents the sum of thermal Joule heating terms and kinetic energy transfer to the thermosphere, and thus the actual rate of heating of the neutrals. At this latitude energy is transferred to the thermosphere at all local times (particularly during local times of enhanced ion production). The discrepancy of both lines highlights the need to consider neutral winds when calculating auroral energy deposition rates. For details see Section 2.3. (For interpretation of the references to colour in this figure legend, the reader is referred to the web version of this article.)

The purely thermal component of Joule heating, q^*_{Joule} (shown as height-integrated quantity by the dashed blue line in Fig. 3), responds simultaneously to changes in conductance, with a similar delay to the precipitation flux. However, as discussed in Section 2.3 the actual heating rate, q_{Joule}, in the atmosphere due to Pedersen and Hall currents needs to take into account the neutral wind velocities as well and is shown in Fig. 3 as solid blue line. Values range from 13.9 mW m^{-2} at 00:00 h SLT to 72 mW m^{-2} at 07:20 h SLT. As a result of westward neutral winds the maximum in Joule heating thus interestingly occurs before the maximum in electron precipitation. This highlights the importance of considering neutral winds when calculating auroral energy deposition rates.

We furthermore note in the figure that height-integrated thermal Joule heating exceeds the height-integrated total Joule heating at all local times, implying that energy is transferred to the thermosphere throughout the day. The difference between the solid and dashed blue curves is larger during local times of enhanced ion production. Following Eq. (11) with Eqs. (7) and (8) it can be shown that under the assumption of $E_\phi = 0$ (as is the case in our simulations), the sign of the expression $[\sigma_P u_\phi - \sigma_H u_\theta \sin(I)]$ determines whether Joule heating is enhanced (positive sign) or reduced (negative sign) due to neutral winds. While we find the sign of this term to become positive in parts of the bottomside ionosphere, it is negative throughout the ionospheric peak region and above. In a height-integrated sense, thus, energy is at that particular latitude transferred to the thermosphere. At other latitudes (not shown) the energy flow locally becomes opposite to that.

3. Simulation results

Simulations R15 and R19 serve as representative cases for average levels of magnetospheric forcing under equinox and solstice conditions, respectively. Comparisons with ionosphere and thermosphere observations are used to validate these simulations. In Section 3.5 we explore the sensitivity of Saturn's upper atmosphere to changes in magnetosphere forcing by analysing the results of all simulations listed in Table 1.

3.1. Ionosphere

Vertical profiles of noontime ionospheric plasma densities are shown in Fig. 4 for the case of R15. The left panel shows profiles in the region of maximum electron precipitation (78°) while the right panel shows densities at the sub-solar point (latitude 0°). Black lines denote the total electron density, blue lines are H^+ and red lines H_3^+ densities. Not shown individually are profiles of other ions calculated in the model, namely H_2^+, CH_3^+, CH_4^+, CH_5^+, H_2O^+ and H_3O_+. The hydrocarbon densities populate the bottomside ionosphere, accounting for most of the electron density below around 1000 km altitude.

Calculated electron densities are about a factor of 10 larger in the auroral region than at the equator. Furthermore, the principal ion at the equator is H_3^+ while in the auroral region it is H^+. This difference is primarily due to differences in neutral composition, specifically the presence of water at equatorial latitudes. As shown in Fig. 1, we assume a water influx over the equator and ignore water chemistry poleward of around 40° latitude. H_2O is particularly effective in removing H^+ from the ionosphere via the charge-exchange reaction given in Eq. (1) which generates an ionosphere richer in molecular ions and depleted in H^+. Ionisation rates for 10 keV electrons peak in the lower ionosphere near 800 km above

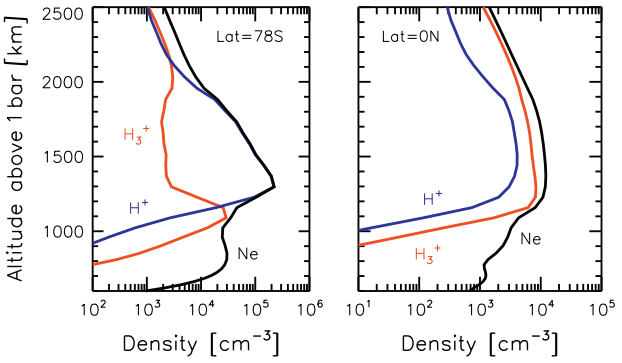

Fig. 4. Vertical profiles of plasma densities at noon in Saturn's ionosphere as calculated in simulation R15 (see Table 1) for the auroral region (78°S latitude, left panel) and equatorial region (0° latitude, right panel). Black lines denote the total ion (and thereby electron-) densities, blue lines are H^+ and red lines H_3^+ densities. To eliminate any effects of differing thermal structures at low and high latitude we applied the same (auroral) pressure level to altitude mapping for both auroral and equatorial cases. In the auroral region which is dominated by electron precipitation, H^+ ions constitute the main ionospheric peak, while at low latitudes the additional influx of water (see Fig. 1) leads to H_3^+ being the dominant ion. The bottomside ionosphere is dominated by hydrocarbon ions (CH_3^+, CH_4^+, CH_5^+) and water ions (H_2O^+, H_3O^+), not shown here individually but only in terms of their total density (black line). (For interpretation of the references to colour in this figure legend, the reader is referred to the web version of this article.)

the 1 bar level (Galand et al., 2011), explaining the bottomside secondary maximum in electron densities in the left panel.

Fig. 5 shows the peak electron densities in Saturn's ionosphere as a function of latitude. The "plus" and "star" symbols are values observed by the Cassini RSS experiment for dusk and dawn conditions, respectively (Nagy et al., 2006; Kliore, 2009). Blue and red lines are calculated peak electron densities from simulations R15 (equinox) and R19 (southern hemisphere summer), respectively, for dusk (solid lines) and dawn (dashed) conditions. The RSS observations were made between 2005 and 2008 when Saturn was transitioning from southern hemisphere summer to near-vernal equinox conditions.

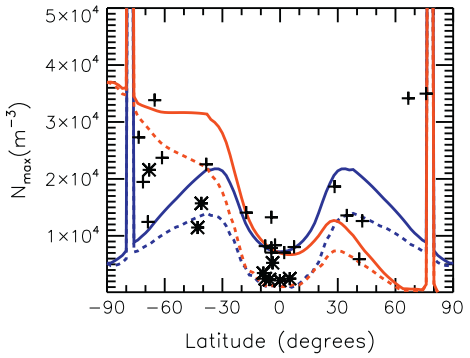

Fig. 5. Latitudinal variation of peak electron densities in Saturn's ionosphere, as observed by the Cassini RSS experiment for dusk (plus symbols) and dawn (star symbols) conditions (Nagy et al., 2006; Kliore, 2009). Super-imposed are peak electron densities from simulations R15 (equinox; blue) and R19 (southern hemisphere summer; red) for dusk (solid lines) and dawn (dashed). The red and blue lines at low and mid latitudes encompass the range of peak densities produced by solar EUV radiation at different seasons. Our calculations reproduce well the observed differences between dusk and dawn densities which are particularly prevalent in the low and mid-latitude regions where H_3^+ as relatively short-lived ion dominates. To-date no radio occultation observation has measured the auroral ionosphere. The dominance of chemical processes over dynamics implies that dynamics are ineffective in redistributing plasma densities outside of the regions of particle precipitation, generating the sharp boundaries seen in the region of the auroral ovals. (For interpretation of the references to colour in this figure legend, the reader is referred to the web version of this article.)

Our calculated values for equinox (blue) and solstice (red) capture the range of observed values, thus validating our simulations and furthermore indicating that the observed trends between 2005 and 2008 can be accounted for by changes in solar ionisation. At low latitudes our calculations reproduce well the observed differences between dusk and dawn densities. This validates our calculated equatorial ion composition shown in Fig. 4 (right panel), as the dominance of H_3^+ there generates sufficiently short ion recombination times to produce the observed dawn–dusk asymmetry. The range of observed peak electron densities is well captured by our calculations.

To-date radio occultations have not yet observed Saturn's ionosphere within the auroral oval. For clarity, modeled auroral electron density values are not fully captured with the chosen axis range in Fig. 5. Calculated peak densities at latitude 78° at dusk/dawn (06:00/18:00 SLT) are 2.2×10^5 cm^{-3}/2.0×10^5 cm^{-3} for the equinox simulation (R15, blue) and for solstice (R19, red) they are 2.4×10^5 cm^{-3}/2.2×10^5 cm^{-3} in the summer hemisphere (78°S) and 2.2×10^5 cm^{-3}/2.0×10^5 cm^{-3} in the winter hemisphere (78°N). Thus, seasonal differences in solar ionisation in the auroral region near the 06:00/18:00 SLT sectors amount to no more than around 10% of the local plasma density.

Despite the longer chemical lifetimes of H^+ relative to H_3^+, chemistry still dominates over dynamics. As calculated by Moore et al. (2004), the overall chemical lifetime of Saturn's ionosphere below 2500 km is $\tau_C \leqslant 10^{-2}$ s. Meridional wind speeds in the auroral region (discussed in Section 3.3) are below 200 m s^{-1}, giving an approximate transport time scale of $\tau_u \approx 10^3$ s, considerably longer than τ_C. Diffusive time scales for ions are around 10^5 s near the ionospheric peak. Thus the ionosphere of Saturn near the peak is approximately in photochemical equilibrium. Furthermore, the large inclination angles of the **B** field at high latitudes imply primarily vertical redistribution of plasma by horizontal neutral winds. Thus, horizontal thermospheric winds are ineffective in redistributing plasma densities to regions outside of the regions of particle precipitation, giving rise to the sharp boundaries between regions with and without precipitation seen in Fig. 5.

3.2. Thermosphere temperatures

Diurnally-averaged thermospheric temperatures, as calculated in simulation R15, are presented in Fig. 6 for the southern hemisphere (with those in the northern hemisphere being identical). We find daily variations of polar temperatures to be less than 6 K and thus virtually negligible, despite the strong diurnal variation of electron precipitation and thereby Joule heating (Fig. 3). The reasons for this are the long thermal time scales in Saturn's upper atmosphere combined with the fast planetary rotation rate. This justifies discussing diurnally-averaged quantities hereafter.

To-date a single polar exospheric temperature value for Saturn has been published from UV stellar occultations and yielded an exospheric temperature of 418 ± 54 K at 82°S (Vervack and Moses, 2012). Temperatures poleward of 75° latitude above the 10^{-5} mbar level in our calculations reach between 350 and 500 K, consistent with the value of Vervack and Moses (2012) and the range of observed auroral H_3^+ temperatures on Saturn of (380–420) ± 70 K (Melin et al., 2007). Thermospheric temperatures poleward of 80° decrease slightly (⩽50 K) when moving to higher levels in the atmosphere above 10^{-5} mbar. This decrease, as will be shown later, is associated with adiabatic cooling due to atmospheric expansion there. Thus we find the thermosphere to be approximately isothermal above 10^{-5} mbar to within ~50 K, implying that observed H_3^+ temperatures (Stallard et al., 1999; Melin et al., 2007) are almost the same as exospheric temperatures in polar regions on Saturn. The same is suggested by the similarity of exospheric temperatures inferred from Voyager UVS observations at 82°S of

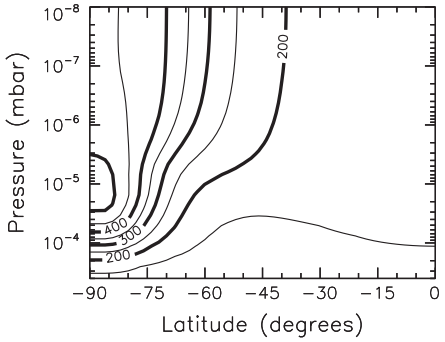

Fig. 6. Local time-averaged temperatures in Saturn's upper atmosphere (southern hemisphere only), as calculated by the STIM GCM in simulation R15 (see Table 1). The ionospheric peak height at auroral latitudes of 1300 km (Fig. 4) corresponds to the 5×10^{-6} mbar pressure level. Diurnal temperature variations at all latitudes and pressures are below ~6 K and hence negligible compared with latitudinal variations. Whilst auroral temperatures are in good agreement with observations, the low and mid-latitude temperatures are considerably colder than observed values, highlighting our current lack of understanding of the energy balance in Saturn's thermosphere at low and mid latitudes, commonly referred to as the "energy crisis", which is similarly present for Jupiter and other Gas Giants.

418 ± 54 K (Vervack and Moses, 2012) to temperatures inferred from ground-based observations of H_3^+ IR emissions of 400 ± 50 K (Melin et al., 2007), even though these observations were not made at the same time. Our calculated polar temperatures in R15 thus agree well with observations.

At lower latitudes our calculations do not capture observed values well. Fig. 6 shows that exospheric temperatures decrease from around 450 K near the pole to around 180 K near the equator. Voyager 2 UVS occultations of δ-Sco suggested an exospheric temperature of 420 ± 30 K near 29.5°N (Smith et al., 1983), while a recent reanalysis of Voyager UVS data inferred a value of 488 ± 14 K (Vervack and Moses, 2012). These and other observations suggest low and mid-latitude exospheric temperatures on Saturn to be of the order of 450 K, roughly twice the value shown in Fig. 6. Our model is presently unable to reproduce observed low and mid-latitude exospheric temperatures on Saturn, illustrating that magnetospheric energy is not being transported from the polar to the equatorial regions. This is related to Saturn's fast rotation rate and the sub-corotation of the auroral thermosphere, which ultimately generates a meridional wind transporting energy from equator to pole in the deep atmosphere, thus cooling down the equatorial regions (Smith et al., 2007). However, since this study is concerned with polar temperatures only we will defer discussion of the equatorial temperature problem to future investigations.

3.3. Dynamics and composition

Auroral forcing directly controls polar thermospheric temperatures through the effects of Joule heating (see Section 3.4). Additionally, the associated ion drag and pressure gradients have a profound influence on thermospheric winds, which in turn also control the energy balance and thus temperatures. Fig. 7 shows vertical profiles of diurnally-averaged meridional (left panel), zonal (middle panel) and vertical winds (right panel). Local time variations in all wind components above the 10^{-5} mbar level are below 1%, making the display of diurnally-averaged quantities there plausible. In the deeper atmosphere at and below 10^{-5} mbar however the ion–neutral momentum coupling is more efficient and causes considerable local time variations in neutral wind velocities. There the displayed diurnal averages do not fully capture the wind behaviour, which we will discuss separately below.

Fig. 7 displays thermospheric wind velocities in the southern hemisphere for a near-auroral latitude of 82°S (solid line), high mid-latitude of 60°S (dashed) and low mid-latitude of 40°S (dotted). Velocities are defined as positive southward (here, poleward), eastward and upward. In the region poleward of the auroral oval (solid line) meridional winds near 10^{-5} mbar are directed poleward, away from the region of Joule heating. At levels above 4×10^{-7} mbar they reverse direction and blow away from the pole, towards the equator. Equatorward winds in the upper thermosphere persist towards mid-latitudes as well (dashed and dotted lines), but decreasing from around 200 m s^{-1} near the pole to around 40 m s^{-1} at mid-latitudes and zero at the equator (not shown). The wind pattern is symmetric in both hemispheres and thus indicates a global meridional circulation cell driven at polar latitudes and consisting of a large pole-to-equator circulation in the upper thermosphere followed by a return flow at lower levels.

The polar forcing via ion drag generates strong westward (sub-corotating) winds at peak velocities of around 1300 m s^{-1} near 82° latitude and ~1600 m s^{-1} near 78° (not shown). In order to relate zonal wind velocities near the ionospheric peak to the degree of corotation of the upper atmosphere, Fig. 8 shows latitudinal profiles of the atmospheric angular velocity relative to Saturn's rotational velocity, ω/Ω_S. The solid black line displays the magnetospheric plasma angular velocity of Cowley et al. (2004)

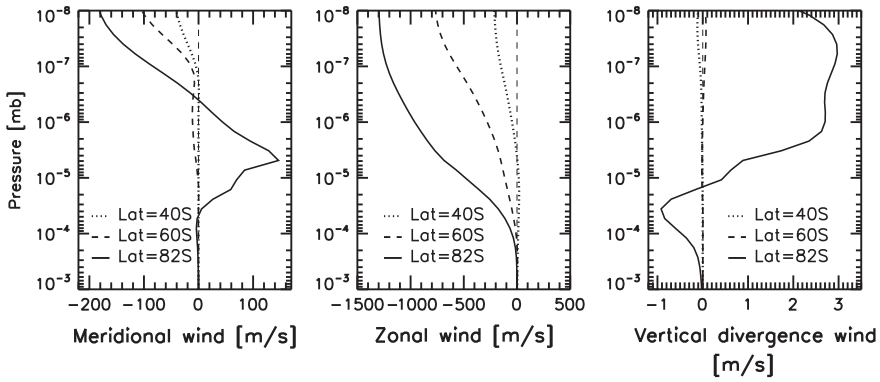

Fig. 7. Vertical profiles of meridional (left panel), zonal (middle panel) and vertical divergence (right panel) thermosphere winds in the southern hemisphere as calculated in simulation R15. Values are shown for near-auroral latitude of 82°S (solid line), high mid-latitude of 60°S (dashed) and low mid-latitude of 40°S (dotted). Velocities are defined as positive southward, eastward and upward. The ionospheric peak height at auroral latitudes of 1300 km (Fig. 4) corresponds to the 5×10^{-6} mbar pressure level. The polar forcing in our simulations generates strong westward (sub-corotating) winds and considerable upwelling above the ionospheric peak (near 10^{-5} mbar) and downwelling below. The forcing generates southward (poleward) winds near the ionospheric peak which result from Coriolis accelerations of the strong westward jets. At higher altitudes the pressure gradients drive meridional winds northward (equatorward). Polar forcing causes the entire atmosphere to sub-corotate, though at a decreasing rate towards the equator. At 60°S (dashed line, middle panel) the thermosphere near the ionospheric peak co-rotates with the planet at ~98%.

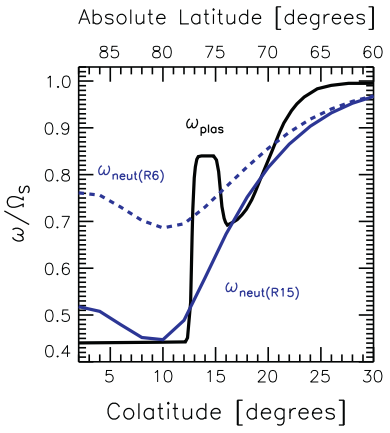

Fig. 8. Angular velocity of plasma in Saturn's magnetosphere (black line), as assumed by Cowley et al. (2004) and mapped into the polar atmosphere. Using a magnetospheric current model, Cowley et al. (2004) inferred from this profile the current densities and electric field that is mapped into the ionosphere and used as polar forcing in our simulations (shown as solid line in Fig. 2). Blue lines denote the thermospheric response to this polar forcing, showing the thermosphere's angular velocity near the peak ionospheric density in simulations R6 and R15 (dashed and solid lines, respectively). The stronger sub-corotation in R15 (solid line) is due to the higher conductances (11.2 mho (R15) versus 1.4 mho (R6)) which are caused by the enhanced particle flux (0.62 mW m^{-2} (R15) versus 0.12 mW m^{-2} (R6)). The more conducting ionosphere in R15 can more efficiently transfer angular momentum to the magnetosphere. (For interpretation of the references to colour in this figure legend, the reader is referred to the web version of this article.)

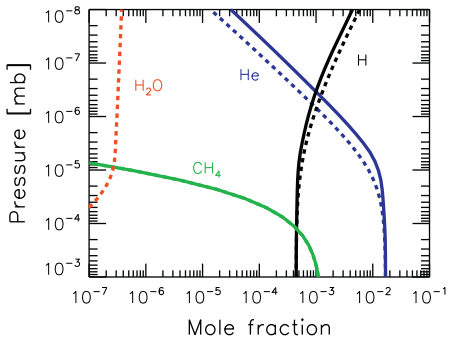

Fig. 9. Vertical profiles of neutral gas mole fractions in simulation R15. Solid lines denote mixing ratios at auroral latitude (78°) and dashed lines are for equatorial latitude (0°). Not shown is the principal gas, H_2, which has a mole fraction close to 1. No H_2O is present at auroral latitudes since we specify a topside influx of H_2O only at low latitudes. Mole fractions of CH_4 are almost identical at both latitudes. Upwelling over the auroral region causes the heavier main gas in the upper thermosphere (He) to be enhanced and the lighter gas (H) to be depleted.

from which the electric field used in our simulations (Fig. 2) was derived. The solid blue line is the atmosphere's diurnally-averaged angular velocity near the ionospheric peak.

The magnetospheric sub-corotation via electric fields mapped into the upper atmosphere is related to sub-corotation of the upper atmosphere with $\omega/\Omega_S \approx 0.45$ near 78° latitude in simulation R15 (high precipitation; solid blue line in Fig. 8). The magnitude of ω/Ω_S is affected by the conductivity of the ionosphere. In simulation R6 (low precipitation, dashed line), the peak incident electron flux is around 20% the value of R15, resulting in maximum Pedersen conductances of 1.4 mho in R6 (versus 11.2 mho in R15) and $\omega/\Omega_S \approx 0.60$ in R6. Thus, the lower conductances in R6 lead to a lesser degree of sub-corotation in the atmosphere. At reduced conductances angular momentum is less efficiently transferred from the upper atmosphere to the magnetosphere.

The right panel of Fig. 7 shows vertical divergence winds in Saturn's upper atmosphere. These are wind velocities generated by the divergence of horizontal winds. They represent the motion of atmospheric gases relative to levels of fixed pressure (rather than simple expansion/contraction of the atmosphere) (Rishbeth and Müller-Wodarg, 1999). In our shown simulation (R15) upwelling occurs above the ionospheric peak (near 10^{-5} mbar) and downwelling below.

The vertical divergence wind generates composition changes in the atmosphere relative to pressure levels, which are presented in Fig. 9 for simulation R15. Solid lines represent mole fractions of neutral gases at 78° and dashed curves are mole fractions over the equator. The high latitude upwelling identified in Fig. 7 enhances mole fractions of heavier gases (He, blue) at a given pressure level and reduces those of lighter gases (H, black). We see wind-induced composition changes only above the 10^{-5} mbar pressure level and not below since eddy mixing is the dominant process transporting gases below the homopause (near 10^{-4} mbar in our model) and vertical gradients of mixing ratios are small there. Hence the auroral CH_4 profile (green) is identical to that at the equator. We note that H_2O is present only over the equator since we specified a topside influx of water which peaked over the equator (Fig. 1), so densities at auroral latitudes are negligible. Not shown in Fig. 9 is the dominant gas (H_2) which is given by $(1-\sum_i X_i)$, X_i being the mole fractions of the gases shown in the figure. H_2 mole fractions are close to 1 and, being the principal gas throughout the domain examined, are little affected by vertical motion in the atmosphere.

One important aspect of thermospheric dynamics is the overall transport of gases which they induce. To examine this, Fig. 10 displays the neutral gas mass flux in Saturn's upper atmosphere which results from neutral wind transport of gases in simulation R15. The figure displays height- and longitude-integrated mass fluxes from meridional winds (solid line), zonal winds (dotted) and vertical divergence winds (dashed). Mass fluxes particularly emphasise the importance of dynamics in the lower thermosphere (below the 10^{-5} mbar pressure level) where wind velocities are smaller (see Fig. 7) but mass densities considerably larger than in the upper thermosphere.

Considerable meridional transport occurs in the auroral region, transporting material away from the sub-auroral thermosphere (76–78°) primarily into the polar cap region (poleward of 78°) and to a smaller extent equatorward as well (solid line in Fig. 10). Vertical transport ensures continuity throughout, supplying mass from the deeper atmosphere to the 76–78° latitude region

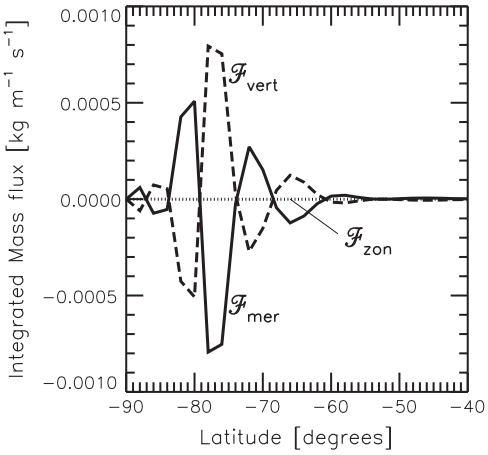

Fig. 10. Neutral gas mass flux in Saturn's upper atmosphere which results from neutral wind transport of gases. The plotted quantities are height- and longitude-integrated mass fluxes due to meridional transport (solid line), zonal transport (dotted) and vertical transport (dashed) in simulation R15.

and transporting material downward in the polar cap area (dashed line in Fig. 10). Note that the downward wind velocities seen in the right panel of Fig. 7 are the dominant cause of this mass flux in the polar cap, by far offsetting the upwelling that is seen at higher levels where the atmospheric densities are considerably lower. Similarly, the meridional wind velocities in Fig. 7 (left panel) near the ionospheric peak are responsible for the bulk of meridional mass transport, rather than the high-altitude winds. Zonal mass fluxes (dotted line in Fig. 10) are negligible (despite the larger zonal wind velocities) since zonal mass density gradients are negligible.

3.4. Energy balance

We now examine the thermospheric energy balance in the auroral region. Fig. 11 shows diurnally-averaged energy terms at (78°S) from simulation R15. Solid lines denote energy sources and dashed lines are energy sinks. The dominant energy source is total Joule heating (green) which includes the contribution from thermospheric neutral winds according to Eq. (11), illustrated also in Fig. 3. As expected for Saturn, and the polar regions in particular, solar EUV heating (black) plays only a minor role. Vertical molecular conduction (blue) acts mostly as an energy sink in the upper thermosphere, conducting the energy down into the lower thermosphere (below around 10^{-4} mbar) where it is deposited and represents a key energy source. Horizontal advection (red) provides the main energy sink in the region of peak heating, due to meridional winds transporting the energy equatorward. In the upper thermosphere energy is transported from the hotter polar region towards the equator, so advection acts as an energy source near 78°. Vertical upward winds provide a further key energy sink in the region via adiabatic cooling (magenta) and vertical advection (cyan). Cooling by H_3^+ IR emissions (grey) plays a minor role on Saturn, unlike what is found on Jupiter (Miller et al., 2010; Bougher et al., 2005; Achilleos et al., 1998).

Our calculations illustrate that dynamics play a key role in controlling the energy balance on Saturn, particularly in the auroral region. The mass flux of Fig. 10 can be regarded as representing the bulk energy flow in the atmosphere and thus ultimately also helps to understand the thermal structure (Fig. 6), including the cold equatorial temperatures. As can be inferred from Fig. 10, auroral (magnetospheric) energy is transported by meridional winds primarily into the polar cap region, explaining the temperature maximum there (Fig. 6). Equatorward energy transport is negligible despite the upper thermosphere pole-to-equator winds (left panel of Fig. 7) since those occur in a region where the atmospheric density is considerably lower and hence energetically insignificant.

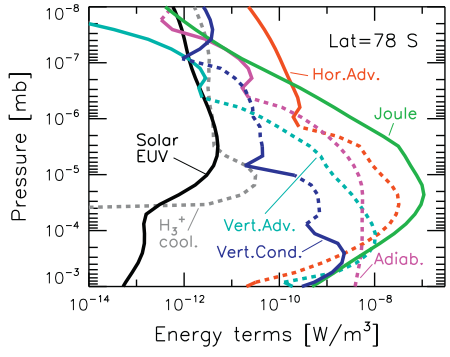

Fig. 11. Diurnally-averaged energy terms in the auroral region (78°S) as calculated in simulation R15. Solid lines denote energy sources and dashed lines are energy sinks. The ionospheric peak height at auroral latitudes of 1300 km (Fig. 4) corresponds to the 5×10^{-6} mbar pressure level. Dominant energy source is Joule heating (green), as given by Eq. (11). Solar EUV heating (black) plays a minor role only. Vertical molecular conduction (blue) acts mostly as an energy sink in the upper thermosphere and energy conducted away from there is deposited in the lower thermosphere below around 10^{-4} mbar where it acts as a source. Horizontal advection (red) provides the main energy sink in the region of peak heating, primarily driven by meridional winds transporting the energy equatorward. In the upper thermosphere energy is transported from the hotter polar region towards the equator, so advection acts as an energy source near 78°. Vertical upward winds provide a further key energy sink in the region via adiabatic cooling (magenta) and vertical advection (cyan). Cooling by H_3^+ IR emissions (grey) plays a minor role only on Saturn, unlike on Jupiter. The figure illustrates the importance of thermospheric dynamics in determining the auroral energy balance. (For interpretation of the references to colour in this figure legend, the reader is referred to the web version of this article.)

3.5. Sensitivity to magnetospheric forcing parameters

Having focused so far on simulations for specific high latitude magnetospheric forcing conditions, we now explore the parameter space of possible electric field and particle precipitation fluxes to examine the atmospheric sensitivity to magnetospheric forcing. Diurnally-averaged temperatures at the peak ionospheric density level (10^{-5} mbar) and latitude 78° from simulations R1–R18 (Table 1) are shown in the upper panel of Fig. 12 as a function of 10 keV electron energy flux and peak electric field strength. As discussed in Section 3.2 (and shown for R15 in Fig. 6) the temperatures may be regarded as representing to within ±50 K exospheric and H_3^+ temperatures. While the values are based on equinox simulations, we found seasonal differences to be insignificant, generating temperature changes of $\leqslant$10 K. The bottom panel of Fig. 12 shows as a function of 10 keV electron energy flux and

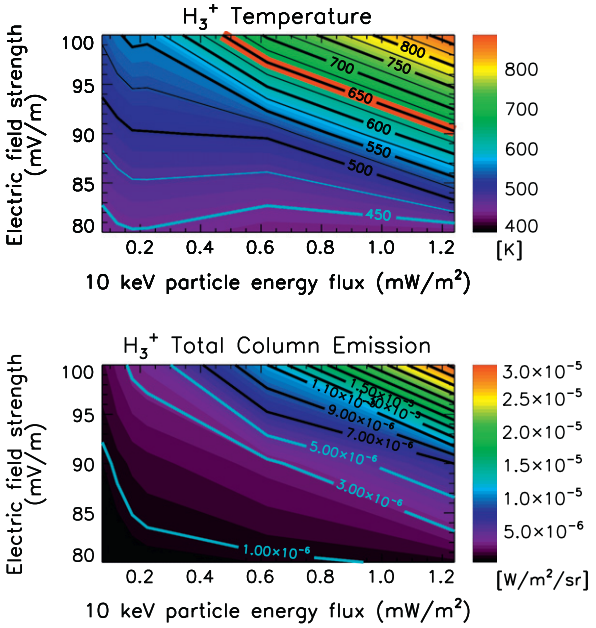

Fig. 12. *Upper panel*: diurnally-averaged thermosphere temperatures (in units of Kelvin) in the auroral region (78°) as a function of magnetospheric forcing parameters, as obtained from simulations R1–R18 (see Table 1). Temperatures are from near the ionospheric peak ($\sim 10^{-5}$ mbar), but are almost identical (within ±50 K) to exospheric temperatures, as can be seen also from Fig. 6 for the particular case of R15. Diurnal temperature variations above the ionospheric peak are below 6 K. While the values in the figure were obtained for equinox conditions, the effect of season is negligible. The thick red line highlights the 650 K contour and approximately separates regions of polar temperatures that have been observed on Saturn ($T \leqslant 650$ K) from those that as yet have not been observed ($T > 650$ K). *Lower panel*: total column emission rates of H_3^+ (in units of W m^{-2} sr^{-1}) calculated from the vertical profiles of H_3^+ densities and temperatures of simulations R1–R18. The full range of emission rates shown ($\leqslant 3 \times 10^{-5}$ W m^{-2} sr^{-1}) is within observed values. (For interpretation of the references to colour in this figure legend, the reader is referred to the web version of this article.)

peak electric field strength the column emission rates of H_3^+ calculated from the vertical profiles of H_3^+ densities and temperatures of simulations R1–R18.

High latitude temperatures in Saturn's upper atmosphere published until recently had values below ~460 K (Melin et al., 2007; Vervack and Moses, 2012), but Melin et al. (2011) and Stallard et al. (2012) have shown that H_3^+ emission may be brighter than previously indicated, and temperatures hotter. Using high resolution Cassini Visual and Infrared Mapping Spectrometer (VIMS) images, Melin et al. (2011) inferred temperatures of a segment of the auroral oval of 440 ± 50 K. Even higher temperatures in Saturn's auroral oval of (563–624) ± 30 K were derived from Cassini VIMS observations by Stallard et al. (2012), so auroral temperatures on Saturn up to around 650 K are within the observed range. The thick red line in the upper panel Fig. 12 highlights the 650 K contour line and thus roughly separates values of polar temperatures that have been observed on Saturn ($T \leqslant 650$ K) from those that as yet have not been observed ($T > 650$ K).

The general trend we find in our simulations is that polar temperatures increase with electric field strength and electron energy flux. At a given energy flux of 1.2 mW m^{-2} the temperatures increase from 450 K to 850 K (by a factor of ~1.9) when increasing the electric field strength from 80 mV m^{-1} to 100 mV m^{-1}. At the lower energy flux of 0.2 mW m^{-2} the temperature changes from 450 K to 550 K, or by a factor of ~1.2 for the same change in electric field. Thus, temperatures are less responsive to electric field variations when ionospheric conductivities (at lower energy fluxes) are smaller. A wider implication of this finding is that Saturn's thermosphere responds less efficiently to magnetospheric input bursts when it is less ionised and more efficiently when in a more ionised state, either due to enhanced electron energy fluxes or due to enhanced solar EUV ionisation (at solar maximum). For the case of magnetic storms, therefore, Saturn's upper atmosphere responds stronger to variations in magnetic field if they were preceded by enhancements in precipitating electron fluxes.

The temperature changes with electron energy flux depend on the electric field strength that was set. For a moderate field strength of 80 mV m^{-1} the temperature is virtually constant when increasing the energy flux from 0.2 to 1.2 mW m^{-2}, while at E = 100 mV m^{-1} it increases from ~550 K to 850 K. Thus we can make the more general statement that for low to moderate electric field strength Saturn's thermospheric temperatures are more responsive to changes in electric field strength than incident energetic electron flux of 10 keV particles. Temperatures are less responsive to changes in energy flux for soft (500 eV) electrons (not shown) as these do not penetrate deep enough into the atmosphere to significantly affect Pedersen and Hall conductances (Galand et al., 2011).

A further finding from the upper panel of Fig. 12 relates to possible restrictions on combinations of electric field strength and 10 keV electron energy flux. The bottom left half of the figure (below the thick red line) represents a range of observed temperatures on Saturn (400–650 K) and thus of "allowed" combinations of electric field strength and particle flux. In contrast, combinations of these two magnetospheric forcing parameters that result in temperatures in the top right part of the figure (above the red line) need to be treated with caution as they produce temperatures in excess of observations. A magnetospheric electric field of ~100 mV m^{-1} mapped into the ionosphere would in combination with at 10 keV electron flux of 1 mW m^{-2} generate thermosphere temperatures of ~800 K, well in excess of observed values. This combination of values cannot thus occur for extended periods on Saturn.

Most temperature constraints on Saturn's polar thermosphere derive from the analysis of H_3^+ emissions, so for a more direct comparison of our simulations we have calculated the total wavelength integrated column emission rates of H_3^+ which are shown in the bottom panel of Fig. 12. We find emission rates to range from (0.1–3.0) × 10^{-5} W m^{-2} sr^{-1}, which is well within the range of observed emission rates. The implication of this is further discussed in Section 4.

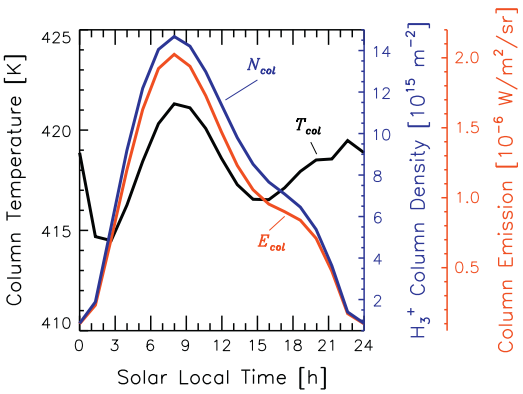

Fig. 13. Column temperature (black), H_3^+ column density (blue) and total IR column emission rate (red) in the auroral region (78°S) as a function of Solar Local Time (SLT), as calculated from results of simulation R15. While temperatures vary little with local time, the H_3^+ column densities change by around a factor of 15 and are the principal cause of local time variations in emissions as well. The peaks near 08:00 SLT are related to the maximum in 10 keV electron energy flux which occurs near 08:00 SLT (black line in Fig. 3). The IR brightness is thus strongly coupled to the incident particle energy flux. (For interpretation of the references to colour in this figure legend, the reader is referred to the web version of this article.)

Finally, it is of interest to relate H_3^+ emissions in Saturn's auroral region to column temperature and H_3^+ density. Fig. 13 displays these quantities as a function of local time for latitude 78°S for the case of simulation R15. Temperature (black) varies by 5 K (or ~1%) while H_3^+ column density changes from around (1—15) × 10^{15} m^{-2}, a factor of 15 variation. The IR column emission (red) changes with local time from a minimum near midnight of 0.1 × 10^{-6} W m^{-2} sr^{-1} to a maximum emission near 08:00 h SLT of 14 × 10^{-6} W m^{-2} sr^{-1}, a factor of 140 variation. We see from this that variations in IR emissions in our simulations are driven primarily by changes in H_3^+ abundance and to a lesser extent by temperature changes. The peaks of all quantities in Fig. 13 near 08:00 SLT are related to the maximum in 10 keV electron energy flux which occurs near 08:00 SLT (black line in Fig. 3) which leads to maximum H_3^+ densities there as well. As the particle ionisation source decreases towards later hours, fast dissociative recombination of H_3^+ leads to an almost immediate decrease of its densities as well. The IR brightness may thus be directly related to the incident particle energy flux or any other major ionisation source.

4. Discussion and conclusions

Our simulations over a range of magnetospheric forcing parameters and seasons successfully reproduce observed ionospheric densities and high latitude temperatures. Analysis of the simulations gives a basic understanding of the processes that control the dynamics and energy balance in Saturn's high latitude coupled thermosphere and ionosphere. We have seen that magnetospheric forcing is responsible for the bulk of energy and mass transport in the atmosphere, driving bulk atmospheric internal mass, momentum and energy redistribution. Joule heating is a major direct contributor to the energy balance, but internal redistribution of this energy by dynamics is crucial as well. Thermospheric winds driven by ion drag and Joule-heating induced pressure gradients play a key role in determining the high latitude energy balance and, more far-reaching, in controlling the global distribution – or lack thereof

– of magnetospheric energy deposited at high latitudes. Under the range of conditions examined in this study the general pattern is consistently that of polar energy being "trapped" at high latitudes and not propagating equatorward. This behaviour results from poleward mass and energy transport in the lower thermosphere, a response previously reported by Smith et al. (2007) with identical conclusions.

We find the sub-corotation of the high latitude thermosphere, which results from magnetospheric plasma sub-corotation and associated electric fields, to be a relatively localised phenomenon which does not extend equatorward of around 65° latitude, beyond which the upper atmosphere is in near co-rotation with the planet. At reduced atmospheric conductances we find angular momentum to be less efficiently transferred from the upper atmosphere to the magnetosphere, thus directly relating precipitating particle mean energy and energy flux to the efficiency of the magnetosphere–atmosphere dynamical coupling processes. Our results are directly dependent upon the assumed magnetospheric plasma velocity profile (and high latitude electric field), so any future revisions of our assumed profile (Fig. 8, black line) in the context of Cassini plasma observations in Saturn's magnetosphere will similarly affect our results in terms of wind velocities, degree of atmospheric co-rotation and thermal structure, moderately shifting with latitude the basic interaction patterns that we identified in our calculations.

Our simulations demonstrate that dynamical coupling to Saturn's ionosphere via ion drag (Eq. (3)) critically controls the pattern of thermospheric winds at high latitudes. Radio science observations of Saturn's ionosphere over the past decades (Atreya et al., 1984; Nagy et al., 2006; Kliore, 2009) have revealed a high degree of variability. Our simulations successfully reproduce the overall latitudinal trend of peak electron densities (Fig. 5), suggesting that the overall neutral–ion collisional coupling calculations are likely to be realistic in our model as well, but in looking at a steady state situation we have not considered the effects of a variable ionosphere. Such observed variations in electron density may have an influence on thermospheric dynamics as well, particularly near the ionospheric peak where we found horizontal winds to vary greatly with local time, responding directly to auroral forcing. A forthcoming second part of this study will examine variability in Saturn's thermosphere–ionosphere system.

Despite strong thermospheric winds at high latitudes we find photochemical equilibrium to hold remarkably well throughout, reducing any role of thermospheric horizontal winds in redistributing ionisation and giving rise to sharp boundaries in ion densities between the auroral and non-auroral regions. Such sharp boundaries may in practice affect the propagation of radio waves through the atmosphere, which may be of relevance during radio occultation measurements at auroral latitudes. To-date no radio science observations have probed the vertical structure of the auroral ionosphere, so our simulations can only be validated there using available H_3^+ IR observations.

In our calculations the dominant ion at the ionospheric peak varies with latitude. At mid and high latitudes including the auroral region H^+ is the principal ion, while at low latitudes it is H_3^+ – a consequence of our assumed influx of H_2O there. The shorter chemical lifetimes of H_3^+ give rise to dawn–dusk asymmetries which have been observed near the equator and are captured remarkably well in our calculations, supporting the notion of an influx of H_2O, most likely from Enceladus. As a result of the dominance of H^+ away from the equator (outside of the region of H_2O influx), chemical lifetimes there increase, thus reducing the chemical sinks and leading to a build-up of ionisation, despite the higher zenith angles at mid latitudes and reduced solar photo-ionisation. The increase of peak ion density away from the equator is entirely consistent with observations by Cassini RSS (Nagy et al., 2006; Kliore, 2009; Moore et al., 2010). At auroral latitudes the main peak in ion production is due to particle ionisation from incident electrons (Galand et al., 2011).

It should be noted, as discussed in Section 2.2, that the H_3^+ densities for any given ionisation rate however depend also on the largely unknown abundance of vibrationally excited H_2. We assumed twice the value of Moses and Bass (2000), but how realistic is this choice? If the incident electron energy and energy flux are known (from UV auroral observations), it may be possible to constrain the abundance of $H_2(v \geqslant 4)$ by comparing observed H_3^+ emission rates and inferred temperature values to the same quantities calculated from simulated atmospheric temperature and H_3^+ profiles. We found temperatures for large electric field strengths and energy fluxes (upper panel of Fig. 12) to partly exceed the observed values, while at the same time the inferred H_3^+ emission rates (bottom panel of Fig. 12) were entirely within observed ranges. This suggests either that our calculations underestimate emission rates or that observed temperatures should in fact be larger for the observed emission rates. The more likely of these options is that our calculations underestimate the ionospheric H_3^+ column densities, which itself may be due to us assuming too low abundances of $H_2(v \geqslant 4)$. Our calculations thus highlight the potential of constraining $H_2(v \geqslant 4)$ abundances in the auroral regions via analysis of H_3^+ emissions.

Despite direct solar EUV heating of Saturn's upper atmosphere representing a minor energy source only, it is however important to note that solar EUV and shorter wavelength radiation is responsible for the majority of ionisation, and thus conductivity, outside of the narrow band of high latitude electron precipitation. This, in turn, may control thermospheric temperatures. As shown in Fig. 2, the region of magnetospheric electric field is considerably wider than the electron precipitation region, so the Joule heating region extends over a much wider region as well. Therefore, solar radiation does affect high latitude temperatures by means of its role as source of ionisation. This causes hemispheric differences in high latitude temperatures at solstice. In our solstice simulation (R19) we find exospheric temperatures averaged from 74°S to 90°S (the summer polar region) of 490 K, while averaging over the same latitude band in the northern (winter) hemisphere gives a value of 430 K. This difference of 60 K is a direct result of enhanced ionisation in the summer hemisphere, leading to stronger Joule heating there. We expect solar cycle variations of high latitude temperatures to lie within the same approximate range, stronger in the summer hemisphere than winter hemisphere, where solar ionisation is considerably weaker. The solar ionisation-induced hemispheric differences in atmospheric conductivity should similarly affect the magnetosphere, highlighting an interesting Sun–atmosphere–magnetosphere coupling chain that deserves more thorough examination in future studies.

Our calculations assumed fixed electrical fields at high latitudes and we did not change these in response to changing conditions in the atmosphere. In principle, enhanced conductivity would lead to more efficient transport of angular momentum from atmosphere to magnetosphere, thus reducing the departure from co-rotation there and the generated electric field which maps into the upper atmosphere. By keeping the electric field constant we assume a continuous supply of new material into Saturn's magnetosphere which is ionised and maintains a continuous lag from co-rotation. This aspect of coupling from atmosphere to magnetosphere is not considered in our model. Smith and Aylward (2008) developed a simple model of Saturn's coupled thermosphere–ionosphere–magnetosphere which considered the feedback from atmosphere to magnetosphere, but assumed a constant ionosphere which did not change in response to thermospheric and magnetospheric conditions. The effects of the feedback on the magnetosphere did however have little influence on the atmosphere behaviour, which is

the focus of our study here. Future developments, though, should ideally focus on an upper atmosphere model such as STIM which considers the full feedback to the magnetosphere as well, thereby providing the possibility of using additional observational constraints from the magnetosphere to validate the calculations.

According to the simulations of our study magnetospheric energy cannot explain the observed thermospheric temperatures at low and mid latitudes. While the "energy crisis" is not the focus of this study, this result emphasises the need to consider thermospheric winds when examining the energy balance, rendering problematic the use of 1-D models which by nature cannot account for winds.

In exploring the parameter space of two magnetospheric forcing parameters, electric field strength and incident particle flux, we have demonstrated that the upper atmosphere observations (in particular, H_3^+ IR emissions) need to be considered when examining Saturn's magnetosphere. Sub-corotation of plasma in the magnetosphere will affect atmospheric temperatures and dynamics, and a multi-instrument analysis is necessary to ensure that any magnetospheric observations are consistent with those of the atmosphere. In applying STIM to an examination of this coupling we have shown that multi-dimensional time-dependent models of the coupled thermosphere–ionosphere–magnetosphere are a powerful and important tool in understanding the exchange of energy and momentum between the regions and in ultimately understanding the global energy balance of Gas Giants within and beyond our Solar System.

Acknowledgments

This work was supported, in part, by a grant from the NASA Planetary Atmosphere Program (PATM) to Boston University. During part of this work I.M.-W. was funded by a Royal Society University Research Fellowship. M.G. and I.M.-W. were partially supported by a UK Science and Technology Facilities Council (STFC) grant to Imperial College London. We would like to thank the International Space Science Institute (ISSI) Bern for their kind hospitality and support of the International Team on Saturn Aeronomy (166), which helped advance through very valuable discussions amongst the Team Members many topics raised in this study. The H_3^+ cooling code has been developed as part of the European Modelling and Data Analysis Facility (EMDAF) under construction by Europlanet RI, the European Union funded network of planetary scientists (see http://europlanet.projects.phys.ucl.ac.uk/europlanetjra3). The authors would like to thank both reviewers of this paper for their constructive and helpful comments.

References

Achilleos, N., Miller, S., Tennyson, J., Aylward, A.D., Müller-Wodarg, I.C.F., Rees, D., 1998. JIM: A time-dependent, three-dimensional model of Jupiter's thermosphere and ionosphere. J. Geophys. Res. 103, 20089–20112.

Anicich, V.G., 1993. Evaluated bimolecular ion-molecule gas phase kinetics of positive ions for use in modeling planetary atmospheres, cometary comae, and interstellar clouds. J. Phys. Chem. Ref. Data 22, 1469–1569.

Atreya, S.K., Donahue, T.M., Nagy, A.F., Waite Jr., J.H., McConnell, J.C., 1984. Theory, measurements, and models of the upper atmosphere and ionosphere of Saturn. In: Gehrels, T., Matthews, M.S. (Eds.), Saturn. University of Arizona Press, pp. 239–277.

Bougher, S.W., Waite, J.H., Majeed, T., Gladstone, G.R., 2005. Jupiter Thermospheric General Circulation Model (JTGCM): Global structure and dynamics driven by auroral and Joule heating. J. Geophys. Res. 110, E04008. http://dx.doi.org/10.1029/2003JE002230.

Cassidy, T.A., Johnson, R.E., 2010. Collisional spreading of Enceladus' neutral cloud. Icarus 209, 696–703. http://dx.doi.org/10.1016/j.icarus.2010.04.010.

Clarke, J.T., Moos, H.W., Atreya, S.K., Lane, A.L., 1981. IUE detection of bursts of H Ly-alpha emission from Saturn. Nature 290, 226–227. http://dx.doi.org/10.1038/290226a0.

Clarke, J.T., Grodent, D., Cowley, S., Bunce, E., Connerney, J., Satoh, T., 2004. Jupiter's aurora. In: Jupiter: The Planet, Satellites, and Magnetosphere. Cambridge Univ. Press, Cambridge, UK, pp. 639–670.

Clarke, J.T. et al., 2009. Response of Jupiter's and Saturn's auroral activity to the solar wind. J. Geophys. Res. 114. http://dx.doi.org/10.1029/2008JA013694.

Cowley, S.W.H., Bunce, E.J., O'Rourke, J.M., 2004. A simple quantitative model of plasma flows and currents in Saturns polar ionosphere. J. Geophys. Res. 109, A05212. http://dx.doi.org/10.1029/2003JA010375.

Cowley, S.W.H. et al., 2008. Auroral current systems in Saturn's magnetosphere: Comparison of theoretical models with Cassini and HST observations. Ann. Geophys. 26, 2613–2630.

Davis Jr., L., Smith, E.J., 1990. A model of Saturn's magnetic field based on all available data. J. Geophys. Res. 95, 15257–15261.

Dungey, J.W., 1961. Interplanetary magnetic field and the auroral zones. Phys. Rev. Lett. 6, 47–48. http://dx.doi.org/10.1103/PhysRevLett.6.47.

Fischer, G., Gurnett, D.A., Zarka, P., Moore, L., Dyudina, U.A., 2011. Peak electron densities in Saturn's ionosphere derived from the low-frequency cutoff of Saturn lightning. J. Geophys. Res. 116, A04315. http://dx.doi.org/10.1029/2010JA016187.

Fuller-Rowell, T.J., Rees, D., 1981. A three-dimensional, time-dependent simulation of the global dynamical response of the thermosphere to a geomagnetic substorm. J. Atmos. Terr. Phys. 43, 701–721.

Fuller-Rowell, T.J., Rees, D., Quegan, S., Moffett, R.J., Codrescu, M.V., Millward, G.H., 1996. A Coupled Thermosphere–Ionosphere Model (CTIM). In: Schunk, R.W. (Ed.), STEP Handbook of Ionospheric Models. Utah State University, Logan, Utah, pp. 217–238.

Galand, M., Moore, L., Charnay, B., Müller-Wodarg, I.C.F., Mendillo, M., 2009. Solar primary and secondary ionization at Saturn. J. Geophys. Res. 114 (A), 06313. http://dx.doi.org/10.1029/2008JA013981.

Galand, M., Moore, L., Müller-Wodarg, I.C.F., Mendillo, M., 2011. Response of Saturn's auroral ionosphere to electron precipitation: Electron density, electron temperature, and electrical conductivity. J. Geophys. Res.. http://dx.doi.org/10.1029/2010JA016412.

Geballe, T.R., Jagod, M.-F., Oka, T., 1993. Detection of H_3^+ infrared emission lines in Saturn. Astrophys J. 408, L109–L112.

Gérard, J.-C., Grodent, D., Gustin, J., Saglam, A., Clarke, J.T., Trauger, J.T., 2004. Characteristics of Saturn's FUV aurora observed with the space telescope imaging spectrograph. J. Geophys. Res. 109, A09207. http://dx.doi.org/10.1029/2004JA010513.

Grodent, D., Radioti, A., Bonfond, B., Gérard, J.-C., 2010. On the origin of Saturn's outer auroral emission. J. Geophys. Res. 115, A08219. http://dx.doi.org/10.1029/2009JA014901.

Gustin, J., Gérard, J.-C., Pryor, W., Feldman, P.D., Grodent, D., Holsclaw, G., 2009. Characteristics of Saturn's polar atmosphere and auroral electrons derived from HST/STIS, FUSE and Cassini/UVIS spectra. Icarus 200, 176–187. http://dx.doi.org/10.1016/j.icarus.2008.11.013.

Hill, T.W., 1979. Inertial limit on corotation. J. Geophys. Res. 84, 6554–6558.

Huestis, D.L., 2008. Hydrogen collisions in planetary atmospheres, ionospheres, and magnetospheres. Planet. Space Sci. 56, 1733–1743. http://dx.doi.org/10.1016/j.pss.2008.07.012.

Judge, D.L., Wu, F.-M., Carlson, R.W., 1980. Ultraviolet photometer observations of the saturnian system. Science 207, 431–434.

Jurac, S., Richardson, J.D., 2007. Neutral cloud interaction with Saturn's main rings. Geophys. Res. Lett. 34, L08102. http://dx.doi.org/10.1029/2007GL029567.

Kaiser, M.L., Desch, M.D., Connerney, J.E.P., 1984. Saturn's ionosphere – Inferred electron densities. J. Geophys. Res. 89, 2371–2376. http://dx.doi.org/10.1029/JA089iA04p02371.

Kliore, A.J. et al., 2009. Midlatitude and high? Latitude electron density profiles in the ionosphere of Saturn obtained by Cassini radio occultation observations. J. Geophys. Res. 114, A04315. http://dx.doi.org/10.1029/2008JA013900.

Kurth, W.S. et al., 2009. Auroral processes. In: Dougherty, M., Esposito, L.W., Krimigis, S.M. (Eds.), Saturn from Cassini–Huygens. Springer, New York, pp. 333–374. http://dx.doi.org/10.1007/978-1-4020-9217-6 (Chapter 12).

Lamy, L., Cecconi, B., Prangé, R., Zarka, P., Nichols, J.D., Clarke, J.T., 2009. An auroral oval at the footprint of Saturn's kilometric radio sources, colocated with the UV aurorae. J. Geophys. Res. 114, A10212. http://dx.doi.org/10.1029/2009JA014401.

Lamy, L. et al., 2010. Properties of Saturn kilometric radiation measured within its source region. Geophys. Res. Lett. 37, L12104. http://dx.doi.org/10.1029/2010GL043415.

Melin, H., Miller, S., Stallard, T., Trafton, L., Geballe, T., 2007. Variability in the H_3^+ emission of Saturn: Consequences for ionisation rates and temperature. Icarus 186, 234–241. http://dx.doi.org/10.1016/j.icarus.2006.08.014.

Melin, H. et al., 2011. Simultaneous Cassini VIMS and UVIS observations of Saturn's southern aurora: Comparing emissions from H, H_2 and H_3^+ at a high spatial resolution. Geophys. Res. Lett. 38, L15203. http://dx.doi.org/10.1029/2011GL048457.

Miller, S. et al., 2006. H_3^+: The driver of Giant Planet atmospheres. Philos. Trans. R. Soc. A 364, 3121–3137. http://dx.doi.org/10.1098/rsta.2006.1877.

Miller, S., Stallard, T., Melin, H., Tennyson, J., 2010. H_3^+ cooling in planetary atmospheres. Faraday Discuss. 147, 283–291. http://dx.doi.org/10.1039/C004152C.

Moore, L., Mendillo, M., Müller-Wodarg, I.C.F., Murr, D., 2004. Modeling of global variations and ring shadowing in Saturn's ionosphere. Icarus 172, 503–520.

Moore, L., Nagy, A.F., Kliore, A.J., Müller-Wodarg, I.C.F., Richardson, J.D., Mendillo, M., 2006. Cassini radio occultations of Saturn's ionosphere: Model comparisons using a constant water flux. Geophys. Res. Lett. 33 (2), 22202. http://dx.doi.org/10.1029/2006GL027375.

Moore, L., Galand, M., Müller-Wodarg, I.C.F., Yelle, R.V., Mendillo, M., 2008. Plasma temperatures in Saturn's ionosphere. J. Geophys. Res. 113, A10306. http://dx.doi.org/10.1029/2008JA013373.

Moore, L., Galand, M., Müller-Wodarg, I.C.F., Mendillo, M., 2009. Response of Saturn's ionosphere to solar radiation: Testing parameterizations for thermal electron heating and secondary ionization processes. Planet. Space Sci. 57, 1699–1705. http://dx.doi.org/10.1016/j.pss.2009.05.001.

Moore, L., Müller-Wodarg, I.C.F., Galand, M., Kliore, A., Mendillo, M., 2010. Latitudinal variations in Saturn's ionosphere: Cassini measurements and model comparisons. J. Geophys. Res. 115 (A), 11317. http://dx.doi.org/10.1029/2010JA015692.

Moses, J.I., Bass, S.F., 2000. The effects of external material on the chemistry and structure of Saturn's ionosphere. J. Geophys. Res. 10 (7), 5013–7052. http://dx.doi.org/10.1029/1999JE001172.

Müller-Wodarg, I.C.F., Mendillo, M., Yelle, R.V., Aylward, A.D., 2006. A global circulation model of Saturn's thermosphere. Icarus 180, 147–160. http://dx.doi.org/10.1016/j.icarus.2005.09.002.

Nagy, A.F. et al., 2006. First results from the ionospheric radio occultations of Saturn by the Cassini spacecraft. J. Geophys. Res. 111, A06310. http://dx.doi.org/10.1029/2005JA011519.

Nagy, A.F. et al., 2009. Upper atmosphere and ionosphere of Saturn. In: Dougherty, M.K., Esposito, L., Krimigis, T. (Eds.), Saturn from Cassini–Huygens. Springer Verlag, ISBN: 978-1-4020-9216-9.

Rishbeth, H., Garriott, O.K., 1969. Introduction to Ionospheric Physics. Academic Press, London.

Rishbeth, H., Müller-Wodarg, I.C.F., 1999. Vertical circulation and thermospheric composition: A modelling study. Ann. Geophys. 17, 794–805.

Sandel, B.R., Shemansky, D.E., Broadfoot, A.L., Holberg, J.B., Smith, G.R., 1982. Extreme ultraviolet observations from the Voyager 2 encounter with Saturn. Science 215, 548–553.

Smith, C.G.A., Aylward, A.D., 2008. Coupled rotational dynamics of Saturn's thermosphere and magnetosphere: A thermospheric modelling study. Ann. Geophys. 26, 1007–1027.

Smith, G.R., Shemansky, D.E., Holberg, J.B., Broadfoot, A.L., Sandel, B.R., McConnell, J.C., 1983. Saturn's upper atmosphere from the Voyager 2 EUV solar and stellar occultations. J. Geophys. Res. 88, 8667–8678. http://dx.doi.org/10.1029/JA088iA11p08667.

Smith, C.G.A., Aylward, A.D., Millward, G.H., Miller, S., Moore, L.E., 2007. An unexpected cooling effect in Saturn's upper atmosphere. Nature 445, 399–401. http://dx.doi.org/10.1038/nature05518.

Stallard, T., Miller, S., Ballester, G.E., Rego, D., Joseph, R.D., Trafton, L.M., 1999. The H_3^+ latitudinal profile of Saturn. Astrophys. J. 521 (2), L149–L152.

Stallard, T., Miller, S., Trafton, L.M., Geballe, T.R., Joseph, R.D., 2004. Ion winds in Saturn's southern auroral/polar region. Icarus 167, 204–211. http://dx.doi.org/10.1016/j.icarus.2003.09.006.

Stallard, T. et al., 2012. Temperature changes and energy inputs in Giant Planet atmospheres: What we are learning from H_3^+ observations. Philos. Trans. R. Soc., in press.

Vasyliūnas, V.M., Song, P., 2005. Meaning of ionospheric Joule heating. J. Geophys. Res. 110 (A). http://dx.doi.org/10.1029/2004JA010615.

Vervack, Jr., R.J., Moses, J.I., 2012, Saturn's upper atmosphere during the Voyager era: Reanalysis and modeling of the UVS occultations, Icarus, submitted for publication.

Waite Jr., J.H., Cravens, T.E., Kozyra, J.U., Nagy, A.F., Atreya, S.K., Chen, R.H., 1983. Electron precipitation and related aeronomy of the jovian thermosphere and ionosphere. J. Geophys. Res. 88, 6143–6163.

Woods, T.N., 2008. Recent advances in observations and modeling of the solar ultraviolet and X-ray spectral irradiance. Adv. Space Res. 42, 895–902. http://dx.doi.org/10.1016/j.asr.2007.09.026.

Woods, T.N. et al., 2005. Solar EUV Experiment (SEE): Mission overview and first results. J. Geophys. Res. 110, A01312. http://dx.doi.org/10.1029/2004JA01076.